

Image Translation for Medical Image Generation – Ischemic Stroke Lesions

Moritz Platscher*, Jonathan Zopes, Christian Federau

*Institute for Biomedical Engineering, University and ETH Zürich, Gloriastrasse 35, 8092
Zürich, Switzerland*

Abstract

Deep learning-based automated disease detection and segmentation algorithms promise to accelerate and improve many clinical processes. However, such algorithms require vast amounts of annotated training data, which are typically not available in a medical context, e.g., due to data privacy concerns, legal obstructions, and non-uniform data formats. Synthetic databases of annotated pathologies could provide the required amounts of training data. Here, we demonstrate with the example of ischemic stroke that a significant improvement in lesion segmentation is feasible using deep learning-based data augmentation. To this end, we train different image-to-image translation models to synthesize diffusion-weighted magnetic resonance images (DWIs) of brain volumes with and without stroke lesions from semantic segmentation maps. In addition, we train a generative adversarial network to generate synthetic lesion masks. Subsequently, we combine these two components to build a large database of synthetic stroke DWIs. The performance of the various generative models is evaluated using a U-Net which is trained to segment stroke lesions on a clinical test set. We compare the results to human expert inter-reader scores. For the model with the best performance, we report a maximum Dice score of 82.6%, which significantly outperforms the model trained on the clinical images alone (74.8%), and also the inter-reader Dice score of two human readers of 76.9%. Moreover, we show that for a very limited database of only 10 or 50 clinical cases, synthetic data can be used to pre-train the segmentation algorithms, which ultimately yields an improvement by a factor of as high as 8 compared to a setting where no synthetic data is used.

Keywords: generative models, image-to-image translation, stroke lesion segmentation, medical image synthesis

*Corresponding author

Email address: platscher@biomed.ee.ethz.ch (Moritz Platscher)

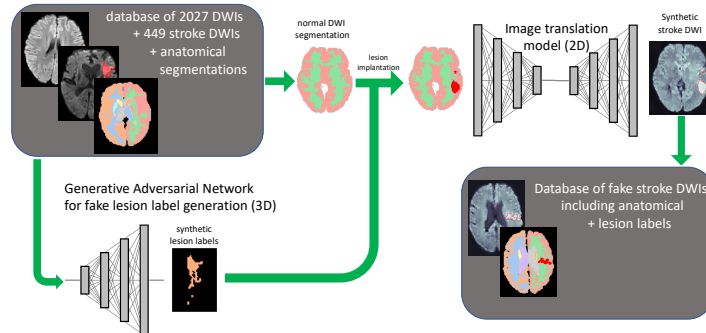


Figure 1: A GAN is trained to produce lesion label maps from a database of 365 manually segmented stroke patients’ DWIs. Using the same 365 pathological volumes and another 2027 healthy brain MR scans, various ITMs are trained to synthesize DWIs from anatomical segmentation masks. The trained ITM can then be used to combine fake lesion labels with healthy brain segmentation masks (real or fake) to produce synthetic stroke DWIs with perfect segmentation labels *by construction*.

1. Introduction

Ischemic stroke (IS) is the second leading cause of death worldwide (WHO, 2018), and if not fatal, frequently results in irreversible brain tissue damage and disabilities. IS is caused by occlusion of blood vessels in the brain and a resulting restricted blood supply to some areas of the brain. Consequently, the success of therapy is closely tied to the time between the onset of symptoms and successful revascularization treatment (Tsai et al., 2018; Saver et al., 2016). Therefore, it is of utmost importance to streamline and optimize the diagnostic process. The present-day gold standard for the identification and quantification of IS lesions is diffusion-weighted magnetic resonance imaging (DWI), on which the infarcted region induces a hyper-intensity compared to normal tissue, corresponding to zones of relative diffusion restriction. Manual segmentation of these areas is a difficult task, e.g., due to the complex lesion geometries, non-trivial changes in signal intensities, varying locations, and possible image artifacts. Machine learning, and deep learning (DL) in particular, holds the potential to automatize such tasks (Hainc et al., 2017; Bernal et al., 2019; Yi et al., 2019). However, the training of DL models requires vast amounts of labeled data, which are typically not available, because e.g., of privacy concerns, incompatible data formats, or because the disease is rare. In addition, manual segmentation of medical images is a task that only experienced radiologists can perform, is tedious, error-prone, and time-consuming. Consequently, large databases of annotated medical images are scarce: For example, the Ischemic Stroke Lesion Segmentation Challenge (ISLES) data set contains 64 IS volumes (Maier et al., 2016). In comparison, the ImageNet database (Stanford Vision Lab, Stanford University, Princeton University, 2016), a popular data set for object recognition in the non-medical area, contains 14 million images.

Synthetic images could bridge the success of DL to medical applications by

augmenting available data sets, or replacing them altogether, circumventing the aforementioned concerns related to data security and availability. Synthetic medical images could be obtained using deep generative models (Goodfellow et al., 2014); however, these methods themselves require large training data sets in order to obtain good results. Moreover, alongside realistic images, the model must provide lesion labels, which is not straightforwardly implemented in standard image synthesis pipelines. Here, we synthesize images relying on image translation models (ITMs), i.e. DL models that transform images from one domain of training data to another domain of training data. In our case we translate semantic segmentation maps to brain DWIs. We envision that the anatomical labels will guide the network to produce sharp images with tissue contrast comparable to the real DWIs. At the same time, the lesion labels of the training set will provide sufficient information to learn a pathology-specific contrast modification. The ITM will learn to generate hyper-intensities inside the lesion labels, while ignoring any (statistically underrepresented) misclassification, such as hyper-intensities outside lesion labels or normal tissue misclassified as belonging to a lesion by the human reader. This has a welcome side effect: the network will produce DWIs with lesions that match the input region labeled as lesion with high confidence, thus providing high quality lesion labels. Using such an approach to obtain synthetic training databases, supervised learning can be applied to segment lesions from normal tissue in clinical data.

The proposed approach is similar in spirit, but more general than (Federau et al., 2020), where synthetic IS volumes were generated by fusing real IS lesion contours into healthy brain DWIs by increasing the voxel intensity within the contour to mimic a lesion. With this approach the authors achieved to increase the Dice similarity coefficient (DSC) from 65% using the clinical data alone to 70% when including 2,000 synthetic images, and even up to 72% using 40,000 synthetic DWIs. An advantage of this approach is that it generates coherent 3D data; however, it is limited combinatorically since there is only a limited number of real lesion labels available. Additionally, there are certain cases where no such labels are available at all, and thus a more generic approach is desirable.

Moreover, (Shin et al., 2018; Yu et al., 2018; Yang et al., 2020) successfully used generative adversarial networks (GANs) to generate synthetic magnetic resonance images (MRIs) to improve brain tumor segmentation. A different approach was used by (Rubin and Abulnaga, 2019): here the authors use an ITM to obtain DWIs from computed tomography (CT) images allowing them to improve the segmentation quality of the ischemic stroke core tissue on CTs augmented with synthetic DWIs.

Here, we try to provide an approach to synthesizing both lesion labels and DWIs from semantic segmentation maps. While the former is realized by IMTs, the lesion labels are generated by a 3D GAN. This allows us to build spatially coherent brain volumes including a lesion label. Moreover, this makes our pipeline scalable in the sense that the GAN can be used to produce an unlimited number of synthetic, yet distinct lesion labels.

We thereby demonstrate that DL-based data augmentation is apt to leverage

the information contained in limited medical data sets and outperform conventional data augmentation techniques, an idea that was coined by (Antoniou et al., 2017) in a non-medical context. We quantify this statement by comparing the DSC of a U-Net (Ronneberger et al., 2015) trained on manually labeled data versus U-Nets trained with the synthetic data, each evaluated on a test set of clinical IS data. To the best of our knowledge, this provides the first comparative study using ITMs for data augmentation in IS lesion segmentation. Finally, we highlight several areas of application for our pipeline.

This paper is structured as follows. In Sec. 2 we describe the data and models that are used in the image synthesis pipeline and detail how to evaluate the results quantitatively. The results of the analysis are presented and discussed in Sec. 3. We conclude in Sec. 4. The Appendix contains supplemental information and technical details on the model architectures.

2. Materials and Methods

We propose to use a pipeline of two consecutive generative models, one for generating realistic stroke lesion labels and another to translate brain segmentation masks into DWIs. This workflow is shown in Fig. 1. In the following we provide a detailed description of the involved data and methods.

2.1. Data

A database of 804 DWIs of patients that presented with symptoms of IS was obtained, for which Institutional Review Board approval was granted by the “Ethikkommission Nordwest- und Zentralschweiz”. This database contains 449 DWI positive cases, i.e. diagnosed IS lesions (mean patient age 72 ± 14 years; 200 left-sided ISs, 193 right-sided ISs, 56 bilateral ISs; 194 female and 255 male), which we use for training (365) and testing (74). Additionally, 85 DWI negative samples are included in the test set, which amounts to 159 test samples in total. A separate database of 2027 healthy DWI scans (mean age 38 ± 24 years; 1088 female, 939 male) is available and is used for the augmentation pipeline. We removed 59 samples due to imaging artifacts.

The pre-processing of the data is kept at a minimum, and includes anonymization of the data, co-registration to the standard Montreal Neurological Institute atlas (McConnell Brain Imaging Centre, Montreal Neurological Institute, 2009), and re-sampling to a standard resolution of $128 \times 128 \times 40$ voxels using ANTs (University of Pennsylvania, Image Computing & Science Lab, 2014). For better stability during training, the top and bottom four slices were cropped. The voxel intensities were clipped at the 99.5th percentile and the background was clipped at an absolute voxel intensity of 35. Finally, we re-scale the intensities to the range $[0, 1]$ for use with the U-Net, and $[-1, 1]$ for the ITMs.

To obtain the anatomical segmentations, we use FreeSurfer as our reference tool (Fischl et al., 2002), and follow (Zopes et al., 2020) to obtain the segmentation masks. The total processing time for the 2027 healthy and 449 stroke cases is of the order of a few hours.

2.2. Image translation

While unconditional GANs have been trained to yield state-of-the-art results on brain DWIs (Hirte et al., 2020), they do not automatically provide ground truth labels for anatomical structures or pathologies. ITMs, on the other hand, are conditional generative models, which generate samples conditional to an input segmentation map. Thus, a perfect ground truth label is available by construction; and moreover, this helps to improve the quality of the generated image by providing boundaries between different instances of a segmentation label. In this section we introduce the ITMs studied in this manuscript, further details can be found in the Appendix.

2.2.1. Pix2Pix

Pix2Pix is a widely used and well-studied ITM, which was first proposed by (Isola et al., 2017) and further developed by (Wang et al., 2018). Pix2Pix is widely accepted as the method of choice for paired image translation, i.e. when the images in two domains come in pairs as it is the case for our database. It has previously been applied successfully to medical data, see e.g. Refs. (Rubin and Abulnaga, 2019; Yang et al., 2020; Wolterink et al., 2017; Choi et al., 2018; Huo et al., 2018; Emami et al., 2018). The original Pix2Pix is based on the U-Net architecture; however, in the high-resolution derivative of the model residual blocks were used (Wang et al., 2018; He et al., 2016). We have trained both architectures but found little difference in quality and therefore used the U-Net based version which converges faster. The loss function for this network is a weighted sum of adversarial loss and L_1 -norm reconstruction loss,

$$\begin{aligned} \mathcal{L} = & \mathbb{E}_y[\log D(y)] + \mathbb{E}_x[1 - \log D(G(x))] \\ & + \lambda \|y - G(x)\|_{L_1}. \end{aligned} \quad (1)$$

In this equation, $\mathbb{E}_{x/y}$ denotes the expectation value taken w.r.t. a batch x or y from one of the two domains, D represents the discriminator network which operates on the target domain and G is the generator network. We consider different values for the reconstruction loss weight λ , since we have found that a value $\lambda = 100$ yields qualitatively more appealing results than the recommended value $\lambda = 10$. For the discriminator architecture we rely on the PatchGAN (Isola et al., 2017; Li and Wand, 2016; Ledig et al., 2017). In contrast to ordinary discriminators, PatchGAN does not output a single number to characterize if an image is real or fake, but does so for patches of the image, thus allowing a more refined feedback for the generator on smaller scales. The large scale, or low-frequency, features are sufficiently well captured by the L_1 loss (Isola et al., 2017).

2.2.2. cycleGAN

A method of unpaired image translation is given by cycleGAN (Zhu et al., 2017). Two generator-discriminator pairs, one for each image domain, allow the model to be trained via a reconstruction loss, translating from domain A to B using the first generator, then back from B to A using the other generator

and computing the pixel-wise (L_1 or L_2 norm) difference between the resulting and the original image. This cycle consistency lends its name to the model and tackles the problem of unpaired data. However, the number of parameters to train is quite vast, reaching 42 million in our setup. In order to handle this large number of free parameters, the model enforces an identity loss, which penalizes deviations of the generators from an identity mapping.¹ Note that cycleGAN has been applied successfully to paired data in medical image generation (Yang et al., 2018; Sandfort et al., 2019).

2.2.3. SPADE

SPADE is the most recent of the ITMs considered in this work. While it has not been widely applied in the medical field, results on ambient images are promising (Park et al., 2019). Furthermore, the SPADE architecture, which is largely identical to a standard GAN, is very economical reducing the number of parameters to train compared to other ITMs. In analogy to GANs (Goodfellow et al., 2014), this model draws a random latent vector which is subsequently upsampled introducing elements of variation in the generative process. The segmentation mask is injected into SPADE normalization layers, which replace the usual batch- or instance-wise normalizations. This guides the model to learn more effectively and converge more rapidly to an optically appealing result (Park et al., 2019).

2.2.4. Training

We have implemented all ITMs as 2D CNNs in tensorflow (Abadi et al., 2016) and trained them on a single GPU (Nvidia Titan RTX 24GB) for 100 epochs on the combined normal and IS clinical data. All models used a batch size of 8 and otherwise are set up as suggested in the references indicated in the previous section. The lesion label generator is trained for 500 epochs on the 3D lesion masks.

We have also attempted to train 3D ITMs, but it turns out that the proposed pipeline guarantees the most economical setup, yet producing coherent 3D brain volumes and IS lesions. The reason is that 3D generative models tend to quickly exhaust available memory capacities such that the image resolution or training batch size are limited. Furthermore, 3D generative models are difficult to train and often do not converge. These issues can be avoided by using 2D ITMs in conjunction with real 3D segmentation maps and 3D fake lesions to guarantee spatial coherence.

2.3. Lesion injection and DWI synthesis

Thus, we use the 2027 healthy brain DWIs and their corresponding anatomical segmentation maps to inject a fake lesion generated by the 3D GAN by

¹Clearly, this identity-loss cannot be used when the input is a multi-channel segmentation map, while the output is a single-channel image. Thus, we do not include an identity loss for training.

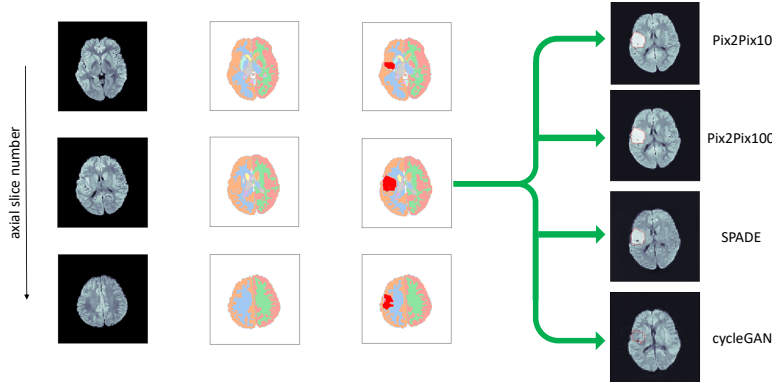


Figure 2: Implantation of a fake lesion and generation of DWIs. *Left*: 3 slices of an original healthy DWI. *Center left*: The segmentation of the original volume. *Center right*: Segmentation map with the implanted lesion label generated by the GAN. *Right*: IS volumes generated from the segmentation maps using different ITMs as indicated.

adapting the label in the parenchyma of the DWI’s segmentation map; however, demanding a minimum lesion volume of 20 voxels. If this requirement is not met, a new lesion mask is generated until a lesion of at least 20 voxels is generated.²

The generated segmentation map is subsequently decomposed into 2D slices and fed into the ITM in order to generate a fake IS DWI. In this manner we obtain a database of 2027 fake DWIs per ITM. Fig. 2 shows an example of this lesion implantation procedure. The left column shows the healthy input DWI volume, whose corresponding semantic segmentation map is shown next to it. The third column shows the segmentation map after implanting a lesion label according to the output of the GAN. Subsequently, we have generated realistic DWIs from axial slices of these 3D segmentation maps using three ITMs, namely Pix2Pix, SPADE and cycleGAN, as shown in the right-most column for one axial slice.

2.4. Evaluation of lesion segmentation

In order to evaluate the performance of the various ITMs quantitatively, we train a segmentation network on the various data sets. This includes the clinical data, clinical data enhanced by the synthetic data, and synthetic data alone. In some cases, we also investigate if the performance can be improved by fine-tuning the model trained on synthetic cases using only a handful of clinical cases. For this purpose we rely on the U-Net architecture proposed by Ronneberger et al. (2015), which has been widely used for various segmentation tasks.

²We have also investigated smaller thresholds, but found no improvement, as this tends to increase the false-positive rate of the segmentation networks.

The U-Net is trained on a combination of cross-entropy loss and DSC,

$$\text{DSC}(A, B) \equiv \frac{2|A \cap B|}{|A| + |B|} = \frac{2 \sum_i A_i B_i}{\sum_i A_i + \sum_j B_j}, \quad (2)$$

where $|\cdot|$ denotes the cardinality of a set and the second equality holds for a pixel-/voxel-based binary segmentation map, and the sums run over all entries. For better comparability, we also report the DSC between the segmentation by two human readers (each with 2 years of experience) of $76.6 \pm 13.9\%$ for the IS database and $76.9 \pm 13.5\%$ for the test set.

Finally, we train the U-Net on clinical, synthetic, and combined data sets for 500 epochs (clinical data alone), or 300 epochs (all others) and using a batch size of 5. To train the U-Net, we also use standard data augmentation techniques, i.e. rotation, translation, sheering and flipping of the input images. Thus, the clinical baseline model can be assumed to reach its best-possible performance.

For training, we exclude all volumes with a volume less than 20 voxels, since the DSC is not stable against false positive predictions when the ground truth has a very small volume. We verify that the trained models are robust against dropping this assumption by evaluating on lesions of all sizes, and also DWI-negative volumes.

3. Results

3.1. Synthetic data generation and qualitative evaluation

We will now have a closer look at the generated images in the right-most column of Fig. 2, which are shown again in Fig. 3. We first remark that, in spite of the 2D nature of the models, the fake DWIs generated by the ITMs display anatomical structures that are coherent in location, shape, and size across the volume, including the lesions.

The two images on the top have been generated using Pix2Pix. Panel 3a was generated using a reconstruction loss weight $\lambda = 10$, while Panel 3b was created using $\lambda = 100$. The results are of good quality, subjectively realistic and, as anticipated, come accompanied by a perfect lesion label. Only closer inspection of a number of volumes reveals that the larger reconstruction loss weight produces slightly sharper images with more details both inside the lesion, as well as in the brain tissue. We have therefore tested both models quantitatively in the following section.

The lesion intensity produced by SPADE (Fig. 3c) is noticeably lower than in the images generated by Pix2Pix, but also the contrast outside the lesion is much lower. While this might seem a disadvantage at first sight, it could actually be beneficial for training a U-Net to reliably detect lesions with lower signal increase. Moreover, the clinical IS DWIs, which the ITMs were trained on, do indeed show less inter-tissue contrast than the healthy brain DWIs. We will return to this issue in Sec. 3.3.

Finally, it can be noticed in Fig. 3d that cycleGAN has failed to recognize and synthesize any lesion hyper-intensity. We have experimented with fine-tuning

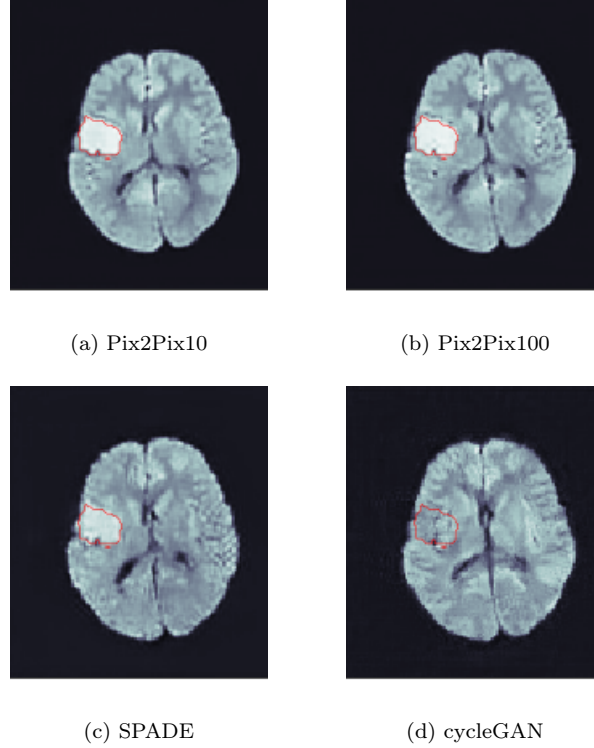


Figure 3: Generated stroke DWIs from the segmentation mask in Fig. 2 using different ITMs.

the model on IS data, training on IS data alone, and modifying the network architecture; however, this result seems to be unavoidable. We speculate that this is closely related to the cycle consistency requirement of cycleGAN, i.e. that the two generators map an image back to itself as close as possible. Similarly, (Zhu et al., 2017) identified ‘failed cases’ which indicate that cycleGAN generalizes poorly to unseen data. Due to this failure, we have excluded cycleGAN from the quantitative analysis, and leave a dedicated study using cycleGAN for data augmentation for future work. We stress that this does not preclude any application of cycleGAN to this task; however, it will require an approach that differs from the one chosen here.

3.2. Training and test set evaluation

To evaluate the quality of the generated images quantitatively, we train a U-Net-based segmentation algorithm (Ronneberger et al., 2015) to learn and extract the lesion segmentation from a given DWI based on the clinical, clinical and synthetic, and synthetic-alone databases for each of the ITMs under consideration. In order to obtain the best benchmark possible, we use standard

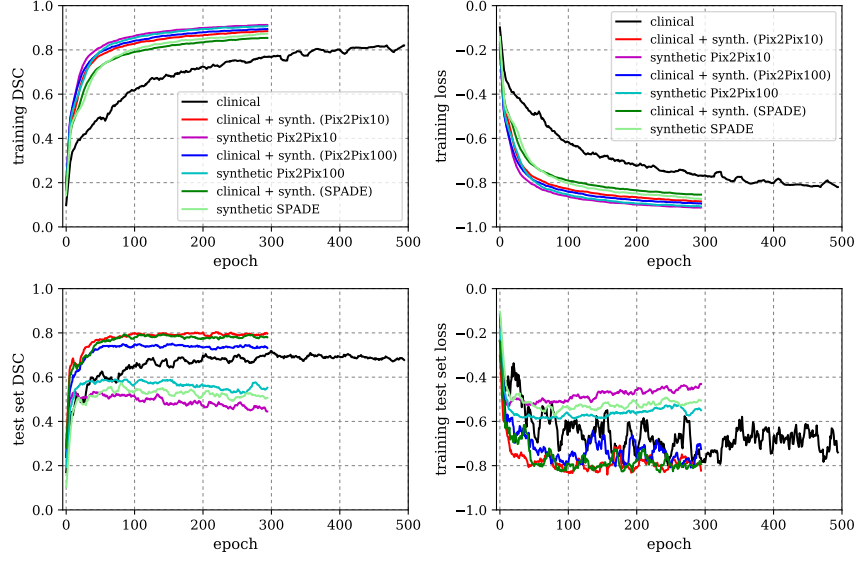


Figure 4: Training of the U-Net on different data sets. The model trained on clinical data alone is trained for 500 epochs, all others for 300. Notice how over-fitting starts already at epoch 100 for the models using synthetic data, while the test set performance of the clinical data keeps improving until epoch 300, after which the test set DSC and loss remain approximately constant. Models trained on synthetic data alone experience a decline in performance once over-fitting sets in, while models trained on synthetic data combined with clinical cases avoid this and reach a plateau.

affine data augmentation including flips, rotations, sheer and translation for the clinical data (Krizhevsky et al., 2012).

The U-Net learning curve on the various data sets and combinations is shown in Fig. 4. In the upper left panel we observe that the training DSC continuously increases, while the DSC evaluated on the clinical test cases in the panel below levels out after 300 epochs for the clinical data set, and around 100 epochs for the combined data sets. For the synthetic data alone, the test set DSC even decreases after epoch 100. The same behavior is observed in the right panels for the combined loss (cross-entropy + DSC). We remark that using synthetic data (with or without the clinical data) helps to stabilize the training and reduces fluctuations in the evaluation DSC and loss.

To compare the models’ performance quantitatively, we consider a range of 100 epochs, chosen at the end of the training history (clinical and combined data), or in the peak performance range (after epoch 50; synthetic alone), to evaluate each trained model on the test set, which has never been seen by any of the involved models. The results are shown in Fig. 5. The upper (orange) box in the ‘clinical baseline’ section is added using the results from (Federau et al., 2020), where a model was trained on 40,000 synthetic IS lesions which were extracted from real IS DWIs and injected into healthy scans by voxel

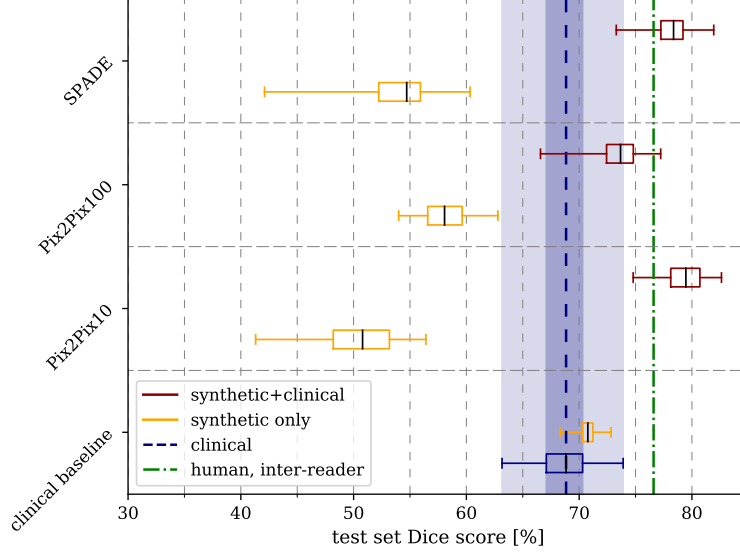


Figure 5: Model comparison. The best performance is achieved when training ITMs on a combined clinical and synthetic data set. The synthetic data sets alone reach DSCs between 50% and 60%.

intensity increase from the same data set, and thus recycling available lesions, which achieved a test set DSC of (mean and standard deviation) $(70.8 \pm 0.6)\%$ (max. 72.8%). In our set-up, the U-Net trained on the clinical data reaches a mean test set DSC of $(68.7 \pm 2.3)\%$ and a maximal DSC of 73.9%. (Federau et al., 2020) reported an inter-reader DSC of 76.9% for the same data set.

Most notably, all U-Nets trained on the combined data outperform the clinical baseline U-Net and we find mean DSCs of $(73.5 \pm 1.9)\%$ [Pix2Pix; $\lambda = 100$], $(78.1 \pm 1.8)\%$ [SPADE], and $(79.4 \pm 1.6)\%$ [Pix2Pix; $\lambda = 10$], respectively. The maximum DSC achieved is a remarkable 82.6% for Pix2Pix with $\lambda = 10$. The other models achieve maximal DSC of 81.9% (SPADE) and 77.2% (Pix2Pix with $\lambda = 100$). This is a key result of our study highlighting that synthetic data does not simply reproduce available information in the training data, but instead interpolates and effectively generalizes the training data.

In contrast to this, the U-Net performs much worse when trained on synthetic data alone, and with much greater variance. We find the test set DSCs $(50.8 \pm 3.1)\%$ [Pix2Pix; $\lambda = 10$], $(54.2 \pm 3.0)\%$ [SPADE], and $(58.0 \pm 1.9)\%$ [Pix2Pix; $\lambda = 100$]. Interestingly, and different from the previous result, the larger reconstruction loss yields better results for Pix2Pix in agreement with our qualitative observation.

3.3. Model fine-tuning

These results indicate that synthetic data alone is not apt to replace the clinical data set. A glance at the voxel intensity distribution in Fig. 6 reveals

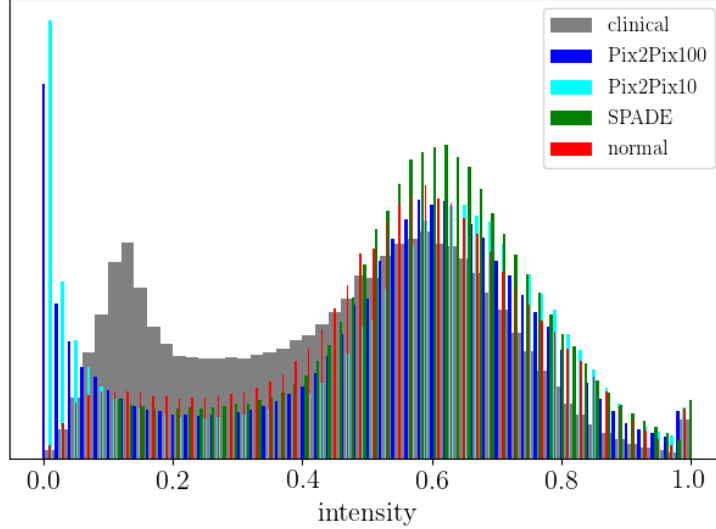


Figure 6: Distribution of voxel intensities. The peak intensities are aligned well; however, the plateau in the clinical data at intensities below 0.5 is not represented in the synthetic data.

why: having trained the ITMs on many normal and only few pathological DWIs, the intensity distribution does not perfectly match that of the clinical IS cases, but rather that of the normal volumes. Nonetheless, the broad features of the distribution are well aligned and the question arises whether one can tune the parameters of the U-Net trained on synthetic data alone on a few clinical cases.

This has been investigated and the results are displayed in Fig. 7, where for each ITM, we train the final model on either 10 or 50 randomly chosen clinical training samples for another 150 epochs.³ In the figure we duplicate the previous result, where the model was trained on synthetic data alone (orange). Subsequently, we show the results after training on 10 (red) and 50 clinical cases (maroon), respectively. Notice the difference between the two distinct architectures, Pix2Pix and SPADE. Increasing the tuning set size from 10 to 50 yields only a minor improvement for SPADE [from $(67.1 \pm 1.5)\%$ for 10 samples to $(70.5 \pm 1.3)\%$ for 50 samples], which after tuning matches the performance of the clinical baseline model within one standard deviation. The situation is quite distinct for Pix2Pix, which for 10 tuning samples is outperformed by the clinical baseline, but tuning it on 50 clinical samples allows Pix2Pix to match ($\lambda = 10$), or even outperform the clinical model ($\lambda = 100$) with a mean DSC of $(69.2 \pm 1.9)\%$ (max. 73.0%) and $(73.7 \pm 1.9)\%$ (max. 77.1%), respectively. Had

³Notice that we do not choose the best performing model, as in practice, one might not have a test set to validate the performance. Thus, we deem it practically more relevant to fine tune the model after 300 training epochs, even if it has over-fitted.

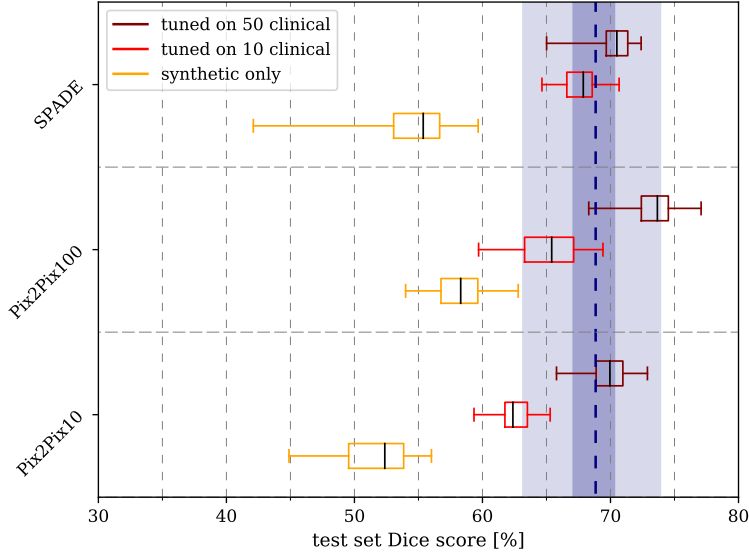


Figure 7: Models trained on synthetic data can be tuned to match the performance of clinical training data with as little as 10 clinical cases, or even outperform it if 50 cases are used.

we trained the U-Net on only 10 [50] cases, the outcome would be much worse: we find a mean DSC of $(8.3 \pm 5.3)\%$ [$(16.4 \pm 3.2)\%$]. In comparison to the models trained on synthetic data and subsequently fine-tuned on 10 [50] clinical cases, this corresponds to an improvement by a factor of approx. 8 [4] for all ITMs.

Therefore, our second key result is that models trained on synthetic data alone do not match the performance of those trained on clinical data sets. However, these models can be fine-tuned if only limited clinical training data is available. This ultimately yields results that are comparable to the clinical baseline model trained on all 365 clinical IS cases allocated for training.

3.4. Discussion

The results of this section illustrate that, depending on the number of available clinical training data, DL-based data augmentation can be used to optimize the achievable model performance. Our findings are summarized in Tab. 1, where we highlight which model is best suited in a given situation.

Training on the clinical set augmented by synthetic data, Pix2Pix with a reconstruction loss weight of $\lambda = 10$ is the choice that yields the best results. Training instead on synthetic data alone, we find that increasing the reconstruction loss weight to $\lambda = 100$ results in the highest DSC. With 10 training samples to fine-tune this model, it yields results comparable to the clinical data set, while it produces better segmentations with only 50 fine-tuning samples. This result matches the qualitative finding that a larger reconstruction loss yields sharper images than the recommended $\lambda = 10$. A more economical model with less

data set	baseline	Pix2Pix10	Pix2Pix100	SPADE
clinical	68.7 ± 2.3	—	—	—
+ all synthetic	70.8 ± 0.6	79.4 ± 1.6	73.5 ± 1.9	78.1 ± 1.8
synthetic	—	50.8 ± 3.1	58.0 ± 1.9	54.2 ± 3.0
+ 10 clinical	—	62.1 ± 1.8	65.1 ± 2.7	67.1 ± 1.5
+ 50 clinical	—	69.2 ± 1.9	73.7 ± 1.9	70.5 ± 1.3

Table 1: Summary of the resulting DSCs (in percent) of the different models trained with various amounts of synthetic data. The last two rows correspond to the fine-tuning procedure described in Sec. 3.3.

adjustable parameters is the SPADE framework, which is attractive for two reasons: First, less trainable weights signify less time for the model to converge and require less training data. And secondly, since SPADE samples from a latent space, it introduces elements of stochasticity as opposed to Pix2Pix, which produces deterministic outputs. Most notably, the model trained on SPADE synthetic data can be fine-tuned on as little as 10 real cases to match the performance found with the clinical data set.

Finally, Fig. 8 shows some examples for segmentations on two clinical test cases. The U-Nets have been trained on clinical data (left-most panels), or on the combined data sets (other panels). Alongside the labeled areas, the ground truth (red) and the corresponding DSC (for the whole volume) are indicated. All models perform well on the large lesion seen in the upper panels of Fig. 8. Conversely, the case shown in the bottom panels, which entails several smaller lesions, is not segmented equally well by all models; especially the U-Net trained only on clinical data produces false positive predictions. This appears to be a common feature and *a posteriori* justifies the lower lesion threshold of 20 voxels, which inhibits too many false-positive predictions. We have also trained models without any restriction on the lesion volume; however, found only worse performance and more false-positive labels.

4. Conclusions & Outlook

We have investigated the applicability of DL-based image-to-image translation models to generalize data augmentation of medical data sets. Our results highlight that DL-based algorithms yield significantly better performance than traditional data augmentation techniques. Our analysis is not the first to report this finding; however, we have – to the best of our knowledge – for the first time performed a comparative analysis, which reveals that certain models are better suited for some tasks depending on the availability of clinical training cases.

This has a number of interesting consequences, as using synthetic data to train disease detection algorithms, e.g. for IS lesion segmentation as in our case,

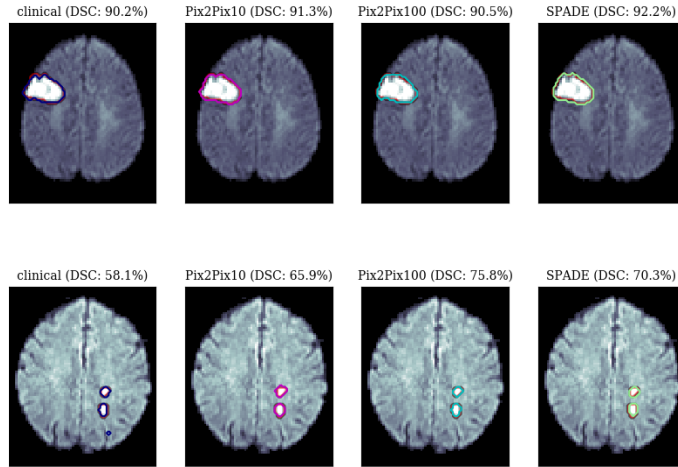


Figure 8: Two segmentation examples: A large lesion (*top*), which is segmented well by all models (DSC > 80%). And a smaller, disconnected lesion (*bottom*). The latter case shows greater variance in DSCs among the models.

avoids any data privacy obstructions. Thus, data can be made available to a much broader audience, which promises to accelerate the advances in machine learning applications in diagnostic medicine. Moreover, this technique can be used to augment available data sets with synthetic data. We have shown that this improves the quality of the segmentation network significantly.

Following up on our results, several directions are conceivable. As we have seen, the synthetic data’s voxel intensity distribution follows that of the healthy MR scans, which are more abundant in the training of the ITMs. A more careful data preparation could provide a more elaborate normalization procedure; however, at the price of fine-tuning the model to a single data set. Alternatively, using the idea of life-long learning (Thrun, 1998; Pan and Yang, 2010), a modified network architecture could be constructed, such as the one by (Karani et al., 2018), which allows users to easily adapt the models to their data, even if acquired under entirely different circumstances. Finally, the proposed pipeline is straightforwardly generalized to other pathologies that can be identified on DWI, but also on other imaging modalities of the entire human body. A particularly interesting question is whether the diagnosis of rare diseases can be improved by augmenting available data sets by artificial data in order to compensate the intrinsic imbalance of the clinical training data.

Acknowledgments

The authors would like to thank Sebastian Kozerke and Thomas Joyce for useful discussions. CF is supported by an Ambizione Fellowship grant

(PZ00P3_173952) of the Swiss National Science Foundation. This work was supported by a SPARK Grant (CRSK-3_190697) of the Swiss National Science Foundation. Calculation for this project were performed in part using support from Google and on a Titan Xp donated by the NVIDIA Corporation.

Appendix A. Model architectures

In this appendix, we describe the model architectures we have used for our DL models. To do so, we use the following abbreviations: Ck is a convolution, CTk a transposed convolution layer with k filters, D is a dropout layer, $(L)ReLU$ is a (leaky) rectified linear unit activation layer, M a max-pooling layer, U a nearest neighbor upsampling layer, BN a batch normalization layer, and IN instance normalization.

Appendix A.1. U-Net

The 3D U-Net (Ronneberger et al., 2015) consists of a downsampling and an upsampling branch, connected by a bottleneck layer. In the downsampling branch, we include 4 blocks $D16-D32-D64-D128$, the upsampling path is $U128-U64-U32-U16-Cn$, where n is the number of segmentation labels, in this case $n = 2$ (IS and non-IS), and the final convolution uses a softmax activation. The downsampling blocks Dk are consecutive layers $Ck-ReLU-D-Ck-ReLU-D-M$ with stride-1 convolutions, while the upsampling blocks Uk are $CTk-BN-ReLU-Ck-ReLU-D-Ck-ReLU-D$ with stride-1 convolutions and stride-2 transposed convolutions. To achieve the U-Net’s characteristic skip connection, the output of each downsampling block is concatenated with the output of the transposed convolution in the upsampling branch at the matching image resolution. Between the two branches, the so-called bottleneck is a block $C256-ReLU-D-C256-ReLU-D$. The dropout rate is 2% and all convolutional kernels are $3 \times 3 \times 3$. The U-Net operates at an image resolution of $128 \times 128 \times 32$ and has a total of $5.6 \cdot 10^6$ trainable parameters. We train the model using a batch size of 5, reflecting memory restrictions.

Appendix A.2. Pix2Pix

The 2D Pix2Pix generator architecture is based on the U-Net, comprising a down- and an upsampling path. The details of the generator are largely identical to the proposed architecture by (Isola et al., 2017). However, we replaced the batch-wise normalization with an instance-wise normalization (Ulyanov et al., 2016). The downsampling path is $D64-D128-D256-D512-D512-D512-D512$, where the downsampling blocks Dk are $Ck-IN-LReLU$. Each convolutional layer contains a 4×4 kernel, stride 2, and is followed by the InstanceNorm. In the upsampling path we use upsampling blocks $U256-U128-U64$, each Uk consists of a sequence of layers $U-Ck-LReLU-D-IN-LReLU$ and stride-1 convolutions with kernel size 4×4 . The downsampling block’s output is concatenated before the final ReLU layer with a leakiness of 0.2. The generator model has a total of $41.8 \cdot 10^6$ trainable parameters, and we use a batch size of 8 for training.

Appendix A.3. SPADE

The SPADE generator samples a latent vector from a 128-dimensional random normal distribution centered at the origin with isotropic variance of unit magnitude. The latent vector is then passed to a dense layer with output size $4 \cdot 4 \cdot 128$ and reshaped into a feature map with dimension $4 \times 4 \times 128$. The following five residual blocks follow the original design by (Park et al., 2019), including the SPADE normalization layers, which process the segmentation maps. The design of each block is SPADE-LReLU-C k -SPADE-LReLU-C k , where the convolutions have a kernel size of 3×3 and unit stride as in the original setup; however, notice that we work with a reduced number of filters k (128-64-32-16-8), the leaky ReLU layers have a slope of 0.2, and each SPADE block is followed by an upsampling layer until the desired resolution of $128 \times 128 \times 32$ is reached. A final 3×3 convolution is added at the end with a tanh activation and a single filter to match the data dimensions. The model is trained with a batch size of 8.

Appendix A.3.1. Discriminator

All ITMs use the PatchGAN discriminator (Isola et al., 2017; Li and Wand, 2016; Ledig et al., 2017), a convolutional network whose output is not a single number as is the case for ordinary discriminator networks. Instead PatchGAN outputs an array of numbers, which, due to the convolutional character of the network, are connected only to a patch of the input image. The size and number of these patches depends on the number of convolutional layers. In the original Pix2Pix setup, where 256×256 images were considered, the receptive field was 70×70 . Here we have chosen three convolutions, C32-IN-LReLU-C64-IN-LReLU-C128-IN-LReLU, which reduces the receptive field from 70×70 to 34×34 – a choice which reflects the fact that the DWI slices under consideration measure 128×128 . The final layer is followed by a stride-one, size-one filter, 4×4 convolution to map to the desired output shape. All other convolutions have kernel sizes 4×4 , stride 2, and filters as indicated; and the leaky ReLU has a slope of 0.2. The discriminator model has a total of 888,898 parameters.

Appendix A.4. Fake lesion generation

We have experimented with several architectures and loss functions and found that a Wasserstein GAN (Arjovsky et al., 2017) with a partial gradient loss (Gulrajani et al., 2017) yields the best results. This model can be trained on 3D lesion masks in a stable manner, and therefore provides the ideal building block for our synthesis pipeline. The output activation of this model is a softmax function, which we transform into a lesion prediction by thresholding at 0.5. The GAN is trained on the 449 lesion masks that are available in the IS database with a batch size of 8 for 500 epochs. We use Instance normalization and Leaky ReLU (leakiness 0.2) activations after each convolution-upsampling step.

References

- Abadi, M., et al., 2016. Tensorflow: A system for large-scale machine learning, in: 12th USENIX Symposium on Operating Systems Design and Implementation (OSDI 16), pp. 265–283. URL: <https://www.usenix.org/system/files/conference/osdi16/osdi16-abadi.pdf>.
- Antoniou, A., Storkey, A., Edwards, H., 2017. Data augmentation generative adversarial networks. *arXiv:1711.04340*.
- Arjovsky, M., Chintala, S., Bottou, L., 2017. Wasserstein GAN, in: Proceedings of the 34th International Conference on Machine Learning, pp. 214–223. <https://www.arxiv.org/abs/1701.07875>.
- Bernal, J., Kushibar, K., Asfaw, D.S., Valverde, S., Oliver, A., Martí, R., Lladó, X., 2019. Deep convolutional neural networks for brain image analysis on magnetic resonance imaging: a review. *Artificial Intelligence in Medicine* 95, 64 – 81. URL: <http://www.sciencedirect.com/science/article/pii/S09333365716305206>, doi:<https://doi.org/10.1016/j.artmed.2018.08.008>.
- Choi, H., Lee, D.S., Initiative, A.D.N., 2018. Generation of structural mr images from amyloid pet: Application to mr-less quantification. *Journal of nuclear medicine : official publication, Society of Nuclear Medicine* 59, 1111–1117. URL: <https://pubmed.ncbi.nlm.nih.gov/29217736>, doi:10.2967/jnumed.117.199414.
- Emami, H., Dong, M., Nejad-Davarani, S.P., Glide-Hurst, C.K., 2018. Generating synthetic cts from magnetic resonance images using generative adversarial networks. *Medical Physics* 45, 3627–3636. URL: <https://aapm.onlinelibrary.wiley.com/doi/abs/10.1002/mp.13047>, doi:10.1002/mp.13047, *arXiv:https://aapm.onlinelibrary.wiley.com/doi/pdf/10.1002/mp.13047*.
- Federau, C., Christensen, S., Scherrer, N., Ospel, J.M., Schulze-Zachau, V., Schmidt, N., Breit, H.C., Maclaren, J., Lansberg, M., Kozerke, S., 2020. Improved segmentation and detection sensitivity of diffusion-weighted stroke lesions with synthetically enhanced deep learning. *Radiology: Artificial Intelligence* 2, e190217. URL: <https://doi.org/10.1148/ryai.2020190217>, doi:10.1148/ryai.2020190217.
- Fischl, B., Salat, D.H., Busa, E., Albert, M., Dieterich, M., Haselgrove, C., van der Kouwe, A., Killiany, R., Kennedy, D., Klaveness, S., Montillo, A., Makris, N., Rosen, B., Dale, A.M., 2002. Whole brain segmentation: Automated labeling of neuroanatomical structures in the human brain. *Neuron* 33, 341 – 355. URL: <http://www.sciencedirect.com/science/article/pii/S089662730200569X>, doi:[https://doi.org/10.1016/S0896-6273\(02\)00569-X](https://doi.org/10.1016/S0896-6273(02)00569-X).

- Goodfellow, I.J., Pouget-Abadie, J., Mirza, M., Xu, B., Warde-Farley, D., Ozair, S., Courville, A., Bengio, Y., 2014. Generative adversarial networks, in: *Advances in neural information processing systems*, pp. 2672–2680. [arXiv:1406.2661](https://arxiv.org/abs/1406.2661). <https://www.arxiv.org/abs/1406.2661>.
- Gulrajani, I., Ahmed, F., Arjovsky, M., Dumoulin, V., Courville, A.C., 2017. Improved training of wasserstein gans. *arXiv e-prints* [arXiv:1704.00028](https://arxiv.org/abs/1704.00028). <http://arxiv.org/abs/1704.00028>,.
- Hainc, N., Federau, C., Stieltjes, B., Blatow, M., Bink, A., Stippich, C., 2017. The bright, artificial intelligence-augmented future of neuroimaging reading. *Frontiers in Neurology* 8, 489. doi:10.3389/fneur.2017.00489.
- He, K., Zhang, X., Ren, S., Sun, J., 2016. Deep residual learning for image recognition, in: *Proceedings of the IEEE Conference on Computer Vision and Pattern Recognition (CVPR)*. [https://www.arxiv.org/abs/1512.03385](https://arxiv.org/abs/1512.03385).
- Hirte, A.U., Platscher, M., Joyce, T., Heit, J.J., Tranvinh, E., Federau, C., 2020. Diffusion-weighted magnetic resonance brain images generation with generative adversarial networks and variational autoencoders: A comparison study. *arXiv e-prints* [https://www.arxiv.org/abs/2006.13944](https://arxiv.org/abs/2006.13944).
- Huo, Y., Xu, Z., Bao, S., Bermudez, C., Plassard, A., Yao, Y., Liu, J., Assad, A., Abramson, R., Landman, B., 2018. Splenomegaly segmentation using global convolutional kernels and conditional generative adversarial networks, p. 8. doi:10.1117/12.2293406.
- Isola, P., Zhu, J.Y., Zhou, T., Efros, A.A., 2017. Image-to-image translation with conditional adversarial networks. *Conference on Computer Vision and Pattern Recognition (CVPR)* [https://www.arxiv.org/abs/1611.07004](https://arxiv.org/abs/1611.07004).
- Karani, N., Chaitanya, K., Baumgartner, C., Konukoglu, E., 2018. A lifelong learning approach to brain mr segmentation across scanners and protocols, in: Frangi, A.F., Schnabel, J.A., Davatzikos, C., Alberola-López, C., Fichtinger, G. (Eds.), *Medical Image Computing and Computer Assisted Intervention – MICCAI 2018*, Springer International Publishing, Cham. pp. 476–484.
- Krizhevsky, A., Sutskever, I., Hinton, G.E., 2012. Imagenet classification with deep convolutional neural networks, in: Pereira, F., Burges, C.J.C., Bottou, L., Weinberger, K.Q. (Eds.), *Advances in Neural Information Processing Systems 25*. Curran Associates, Inc., pp. 1097–1105. URL: <http://papers.nips.cc/paper/4824-imagenet-classification-with-deep-convolutional-neural-networks.pdf>.
- Ledig, C., Theis, L., Huszar, F., Caballero, J., Aitken, A.P., Tejani, A., Totz, J., Wang, Z., Shi, W., 2017. Photo-realistic single image super-resolution using a generative adversarial network, pp. 4681–4690. [https://www.arxiv.org/abs/1609.04802](https://arxiv.org/abs/1609.04802).

- Li, C., Wand, M., 2016. Precomputed real-time texture synthesis with markovian generative adversarial networks, in: Leibe, B., Matas, J., Sebe, N., Welling, M. (Eds.), *Computer Vision – ECCV 2016*, Springer International Publishing, Cham. pp. 702–716. <https://www.arxiv.org/abs/1604.04382>.
- Maier, O., et al., 2016. ISLES 2015 - A public evaluation benchmark for ischemic stroke lesion segmentation from multispectral MRI Medical Image Analysis. <http://dx.doi.org/10.1016/j.media.2016.07.009>. www.isles-challenge.org.
- McConnell Brain Imaging Centre, Montreal Neurological Institute, 2009. MNI human atlas. http://nist.mni.mcgill.ca/?page_id=714. Accessed 08/10/2020.
- Pan, S.J., Yang, Q., 2010. A survey on transfer learning. *IEEE Transactions on Knowledge and Data Engineering* 22, 1345–1359.
- Park, T., Liu, M.Y., Wang, T.C., Zhu, J.Y., 2019. Semantic image synthesis with spatially-adaptive normalization. *Conference on Computer Vision and Pattern Recognition (CVPR)*, 2332–2341 <https://www.arxiv.org/abs/1903.07291>.
- Ronneberger, O., Fischer, P., Brox, T., 2015. U-Net: Convolutional Networks for Biomedical Image Segmentation, in: *Medical Image Computing and Computer-Assisted Intervention (MICCAI)*, pp. 234–241. <https://www.arxiv.org/abs/1505.04597>.
- Rubin, J., Abulnaga, S.M., 2019. Ct-to-mr conditional generative adversarial networks for ischemic stroke lesion segmentation, in: *2019 IEEE International Conference on Healthcare Informatics (ICHI)*, pp. 1–7.
- Sandfort, V., Yan, K., Pickhardt, P.J., Summers, R.M., 2019. Data augmentation using generative adversarial networks (CycleGAN) to improve generalizability in CT segmentation tasks. *Scientific reports* 9, 16884. doi:10.1038/s41598-019-52737-x. <https://europepmc.org/articles/PMC6858365>.
- Saver, J., Goyal, M., Lutg, A., Menon, B., Majoie, C., Dippel, D., Campbell, B., Nogueira, R., Demchuk, A., Tomasello, A., Cardona, P., Devlin, T., Frei, D., Rochemont, R., Berkhemer, O., Jovin, T., Siddiqui, A., Zwam, W., Davis, S., Hill, M., 2016. Time to treatment with endovascular thrombectomy and outcomes from ischemic stroke: A meta-analysis. *JAMA* 316, 1279–1288. doi:10.1001/jama.2016.13647.
- Shin, H.C., Tenenholtz, N.A., Rogers, J.K., Schwarz, C.G., Senjem, M.L., Gunter, J.L., Andriole, K.P., Michalski, M., 2018. Medical image synthesis for data augmentation and anonymization using generative adversarial networks, in: Gooya, A., Goksel, O., Oguz, I., Burgos, N. (Eds.), *Simulation and Synthesis in Medical Imaging*, Springer International Publishing, Cham. pp. 1–11.

- Stanford Vision Lab, Stanford University, Princeton University, 2016. ImageNet. <http://www.image-net.org>. Accessed: 08/10/2020.
- Thrun, S., 1998. Lifelong Learning Algorithms. Springer US, Boston, MA. pp. 181–209. URL: https://doi.org/10.1007/978-1-4615-5529-2_8, doi:10.1007/978-1-4615-5529-2_8.
- Tsai, J., Mlynash, M., Christensen, S., Kemp, S., Kim, S., Mishra, N., Federau, C., Nogueira, R., Jovin, T., Devlin, T., Akhtar, N., Yavagal, D., Bammer, R., Straka, M., Zaharchuk, G., Marks, M., Albers, G., Lansberg, M., 2018. Time from imaging to endovascular reperfusion predicts outcome in acute stroke. *Stroke* 49, 952–957. doi:10.1161/STROKEAHA.117.018858.
- Ulyanov, D., Vedaldi, A., Lempitsky, V.S., 2016. Instance normalization: The missing ingredient for fast stylization. arXiv e-prints [arXiv:1607.08022](https://arxiv.org/abs/1607.08022). <http://arxiv.org/abs/1607.08022>.
- University of Pennsylvania, Image Computing & Science Lab, 2014. Advanced Normalization Tools (ANTs). <http://picsl.upenn.edu/software/ants>. Accessed 08/10/2020.
- Wang, T.C., Liu, M.Y., Zhu, J.Y., Tao, A., Kautz, J., Catanzaro, B., 2018. High-resolution image synthesis and semantic manipulation with conditional gans, in: Proceedings of the IEEE conference on computer vision and pattern recognition, pp. 8798–8807. <https://www.arxiv.org/abs/1711.11585>.
- WHO, 2018. The top ten causes of death. <https://www.who.int/en/news-room/fact-sheets/detail/the-top-10-causes-of-death>. Accessed: 08/10/2020.
- Wolterink, J.M., Leiner, T., Viergever, M.A., Išgum, I., 2017. Generative adversarial networks for noise reduction in low-dose ct. *IEEE Transactions on Medical Imaging* 36, 2536–2545.
- Yang, H., Sun, J., Carass, A., Zhao, C., Lee, J., Xu, Z., Prince, J., 2018. Unpaired brain mr-to-ct synthesis using a structure-constrained cyclegan, in: Stoyanov, D., Taylor, Z., Carneiro, G., Syeda-Mahmood, T., Martel, A., Maier-Hein, L., Tavares, J.M.R., Bradley, A., Papa, J.P., Belagiannis, V., Nascimento, J.C., Lu, Z., Conjeti, S., Moradi, M., Greenspan, H., Madabhushi, A. (Eds.), *Deep Learning in Medical Image Analysis and Multimodal Learning for Clinical Decision Support*, Springer International Publishing, Cham. pp. 174–182.
- Yang, Q., Li, N., Zhao, Z., Fan, X., Chang, E.I.C., Xu, Y., 2020. Mri cross-modality image-to-image translation. *Scientific Reports* 10, 3753. URL: <https://doi.org/10.1038/s41598-020-60520-6>, doi:10.1038/s41598-020-60520-6.

- Yi, X., Walia, E., Babyn, P., 2019. Generative adversarial network in medical imaging: A review. *Medical Image Analysis* 58, 101552. doi:<https://doi.org/10.1016/j.media.2019.101552>. <https://www.arxiv.org/abs/1809.07294>.
- Yu, B., Zhou, L., Wang, L., Fripp, J., Bourgeat, P., 2018. 3d cgan based cross-modality mr image synthesis for brain tumor segmentation, in: 2018 IEEE 15th International Symposium on Biomedical Imaging (ISBI 2018), pp. 626–630. <https://arxiv.org/abs/1810.11654>.
- Zhu, J., Park, T., Isola, P., Efros, A.A., 2017. Unpaired image-to-image translation using cycle-consistent adversarial networks, in: IEEE International Conference on Computer Vision (ICCV), pp. 2242–2251. <https://www.arxiv.org/abs/1703.10593>.
- Zopes, J., Platscher, M., Paganucci, S., Federau, C., 2020. Multi-modal segmentation of 3d brain scans using neural networks <https://www.arxiv.org/abs/2008.04594>.